

# Quantum tele-amplification with a continuous variable superposition state

Jonas S. Neergaard-Nielsen,<sup>1,2</sup> Yujiro Eto,<sup>1,3</sup> Chang-Woo Lee,<sup>4,5</sup> Hyunseok Jeong,<sup>4</sup> and Masahide Sasaki<sup>1</sup>

<sup>1</sup> National Institute of Information and Communications Technology (NICT),  
4-2-1 Nukui-kitamachi, Koganei, Tokyo 184-8795, Japan

<sup>2</sup> Department of Physics, Technical University of Denmark, Fysikvej, 2800 Kgs. Lyngby, Denmark

<sup>3</sup> Department of Physics, Gakushuin University, 1-5-1 Mejiro, Toshima-ku, Tokyo 171-8588, Japan

<sup>4</sup> Center for Macroscopic Quantum Control, Department of Physics and Astronomy,  
Seoul National University, Seoul, 151-747, Korea

<sup>5</sup> Department of Physics, Texas A&M University at Qatar, PO Box 23874, Doha, Qatar

(Dated: November 29, 2012)

Quantum superpositions of coherent states, often referred to as Schrödinger cat states, play an important role in fundamental tests of quantum theory and in quantum information processing and communication tasks, such as coherent-state quantum computing (CSQC) [1–5], metrology [6, 7], and quantum repeater [8]. Optical cat states are now routinely generated in the laboratories. However, real use cases of these tasks have not yet been demonstrated. Here we demonstrate a basic CSQC protocol, where a cat state is used as an entanglement resource for teleporting a coherent state with an amplitude gain, extendable to coherent state qubits. We also show how this can be extended to a loss-tolerant quantum relay of multi-ary phase-shift keyed coherent states. These protocols could be useful both in optical and quantum communications.

Among the various optical implementations of quantum information processing (QIP), coherent-state quantum computing (CSQC) is of special interest for enhancing the performance of advanced optical communications, where information is encoded into coherent states. These are the only pure states that can be transmitted intact through a lossy channel since they are eigenstates of the annihilation operator,  $\hat{a}|\alpha\rangle = \alpha|\alpha\rangle$ . Hence, a simple classical encoding with coherent states – that is, without quantum entanglement – can be the optimal strategy of the transmitter to achieve the ultimate capacity of a lossy optical channel [9]. On the receiver side, the sequence of coherent-state pulses should be decoded by projecting them onto a set of entangled coherent-state bases so as to induce quantum interference in the measurement processes. This can be implemented by first transforming, by CSQC, the received codeword into appropriate superpositions of several possible codewords, followed by a conventional separable measurement [10]. This scheme can realize communication with larger capacity for a given input power, beating the conventional limit of optical communications with homodyne receivers [11]. Although practical implementation of CSQC remains a big challenge, recent progress in generation [12–16] and manipulation [17, 18] of optical Schrödinger cat states makes it realistic to implement its basic building blocks. In this paper, we propose and demonstrate the first operational application of cat states for QIP, where a cat state is used as the entanglement resource for teleporting a coherent state with an amplitude gain. We also propose a new application of this to quantum key distribution (QKD), namely a loss-tolerant quantum relay of multi-ary phase-shift keyed (M-PSK) coherent states that does not assume a trusted node. We present its proof-of-principle demonstration with binary PSK states.

The basic scheme of teleportation from Alice to Bob of

a cat state qubit  $|\psi\rangle_A = c_+|\alpha\rangle_A + c_-|-\alpha\rangle_A$ , which is a variation of the schemes in [19, 20], is depicted in Fig. 1a. Bob prepares a cat state  $|\Phi_-(\beta)\rangle_B = \mathcal{N}_-(|\beta\rangle_B - |-\beta\rangle_B)$  (with normalization  $\mathcal{N}_-$ ) and splits it into an entangled cat state over paths B and C via a beam-splitter (BS)  $\hat{V}_{BC}$  with reflectivity  $R_B$ . He sends one part of it to Alice at port C. She then combines it on an  $R_A$  reflectivity BS with her input  $|\psi\rangle_A$  at port A as

$$|\Psi\rangle_{ABC} = \hat{V}_{AC}|\psi\rangle_A \hat{V}_{BC}|\Phi\rangle_B |0\rangle_C. \quad (1)$$

She finally measures modes A and C by single photon detectors. By conditioning port B on her measurement result, Bob can restore Alice's input.

In order to do so, we impose a condition on the amplitude of the resource cat state,  $\beta = \alpha\sqrt{(1-R_A)/R_A R_B}$ , such that the components at port A turn into either the vacuum or a non-vacuum state. Then, when Alice's detectors register a single photon at port A and nothing at port C – denoted (1,0) – Bob unambiguously obtains the state (see Appendix A)

$$AC\langle 1,0|\Psi\rangle_{ABC} \propto c_+|-\alpha\rangle_B + c_-|\alpha\rangle_B, \quad (2)$$

where  $g = \sqrt{(1-R_A)(1-R_B)/R_A R_B}$  is the gain parameter. By a simple  $\pi$ -phase shift, it can be transformed to Alice's input  $|\psi\rangle_A$ , but with a modified amplitude  $\alpha' = g\alpha$ . This process, previously suggested in [3], we will call *tele-amplification*.

Unfortunately this tele-amplification is vulnerable to losses. Suppose the channel between Alice and Bob is subject to a linear loss  $R_E$ . The amplitude of the resource cat state should then be chosen as

$$\beta = \sqrt{\frac{1-R_A}{R_A R_B (1-R_E)}} \alpha. \quad (3)$$

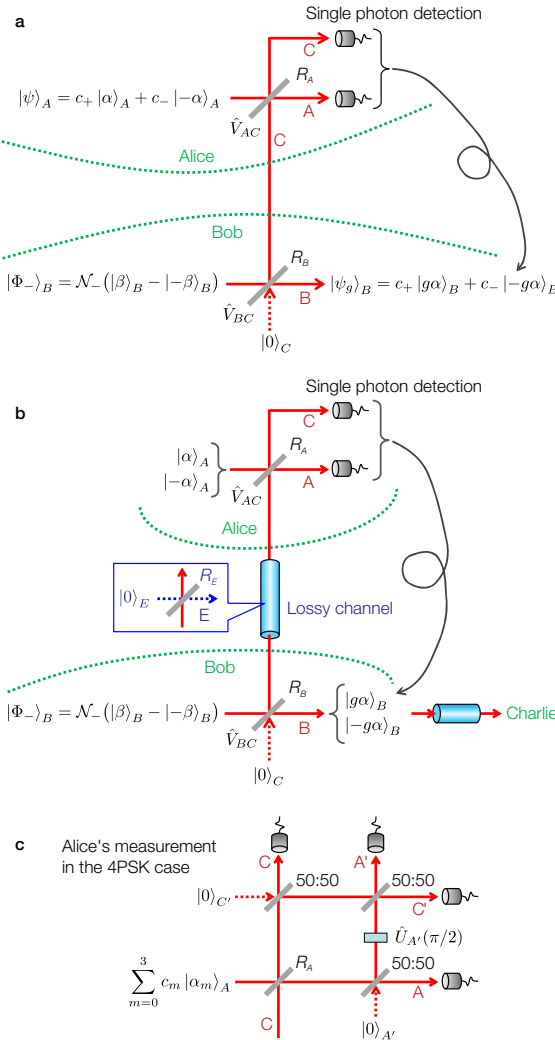


FIG. 1: **Scheme of quantum tele-amplification and quantum relay.** **a** Tele-amplification of binary cat-state in an ideal lossless channel.  $R_A$  and  $R_B$  are the reflectivities of the BSs. **b** Loss tolerant quantum relay.  $R_E$  is the reflectivity of the BS which models the lossy channel. **c** Alice's four-port measurement for the case of 4PSK states.

After conditioning on Alice's detection event (1,0), Bob's state gets entangled with an external mode E as

$$|\psi\rangle_A |0\rangle_E \mapsto c_+ |g\alpha\rangle_B |\varepsilon\rangle_E + c_- |g\alpha\rangle_B |-\varepsilon\rangle_E \quad (4)$$

with the modified gain including the loss rate  $R_E$

$$g = \sqrt{\frac{(1 - R_A)(1 - R_E)}{R_A R_B (1 - R_E)}}. \quad (5)$$

Here  $\varepsilon = \sqrt{(1 - R_A)R_E/R_A(1 - R_E)}\alpha$ . Thus, the output at Bob is generally in a decohered state.

One can, however, see that if Alice's inputs are restricted to classical components, namely  $|\alpha\rangle$  or  $|-\alpha\rangle$ , as in Fig. 1b, the output state can be completely disentangled from the external mode. This means that the coherent states can be tele-amplified faithfully to the target states even through the lossy channel as

$$|\pm\alpha\rangle_A \mapsto |\pm g\alpha\rangle_B. \quad (6)$$

This is referred to as *loss-tolerant quantum relay*. In this context, Bob plays the role of an intermediate node, restores the target states  $|\pm g\alpha\rangle_B$ , and sends them to the terminal node, Charlie.

This simplest binary case can be extended into M-PSK coherent states. Let us show it for the 4-PSK case,  $|\alpha_m\rangle$ , ( $\alpha_m = i^m \alpha$ ,  $m = 0, 1, 2, 3$ ). Bob should prepare a 4-component cat state

$$|\Phi\rangle_B = \mathcal{N} \sum_{k=0}^3 i^k |\alpha_k\rangle_B \quad (7)$$

as a resource state, which is quite challenging, though. This state is beam-split, and is shared with Alice. We set  $R_A = 0.5$ . As in Fig. 1c, Alice performs a four-port single photon detection at paths A, A', C, and C' on this state. Depending on the set of results at the four ports, (A, A', C, C'), the inputs are tele-amplified as

$$\begin{aligned} |\alpha_m\rangle &\mapsto |g\alpha_m\rangle, & \text{for } (0, 1, 1, 1), \\ |\alpha_m\rangle &\mapsto |ig\alpha_m\rangle, & \text{for } (1, 0, 1, 1), \\ |\alpha_m\rangle &\mapsto |-g\alpha_m\rangle, & \text{for } (1, 1, 0, 1), \\ |\alpha_m\rangle &\mapsto |-ig\alpha_m\rangle, & \text{for } (1, 1, 1, 0). \end{aligned} \quad (8)$$

Thus, the simple tele-amplification is performed for the result (0,1,1,1). Moreover the output state can be switched to another element by choosing an appropriate click pattern at Alice (see Appendix B).

The relay function itself can also be realized in a classical way, where Bob at the intermediate node performs an unambiguous state discrimination (USD) on the signal state, reproduces an amplified state for his confident result, and finally resends it to Charlie. This classical relay cannot, however, be applied to a QKD relay node without the trusted node assumption. Consider QKD protocols which use  $M$ -ary coherent states in their implementations, such as B92 and BB84, possibly with strong reference pulses [24–26]. When the intermediate node (Bob) cannot be trusted, being at hand of an eavesdropper (Eve), a significant portion of the information shared by Alice and Charlie leaks to Eve by the USD, degrading the QKD distance and the key rate. In contrast, a quantum relay can be carried out in the fully quantum domain, without Bob's knowing the signal state itself, though at the expense of preparing the entangled cat-state. Similar ideas with entangled photon pairs for single-photon QKD were presented in [21, 22]. So if the QKD protocol is accompanied by an appropriate entanglement verification session, the scheme can be used for a relay without the trusted node assumption. However, for precise quantification of relayed QKD performance of the current scheme, further study on validation of the security proof with added reference pulses as in [24–26] is needed.

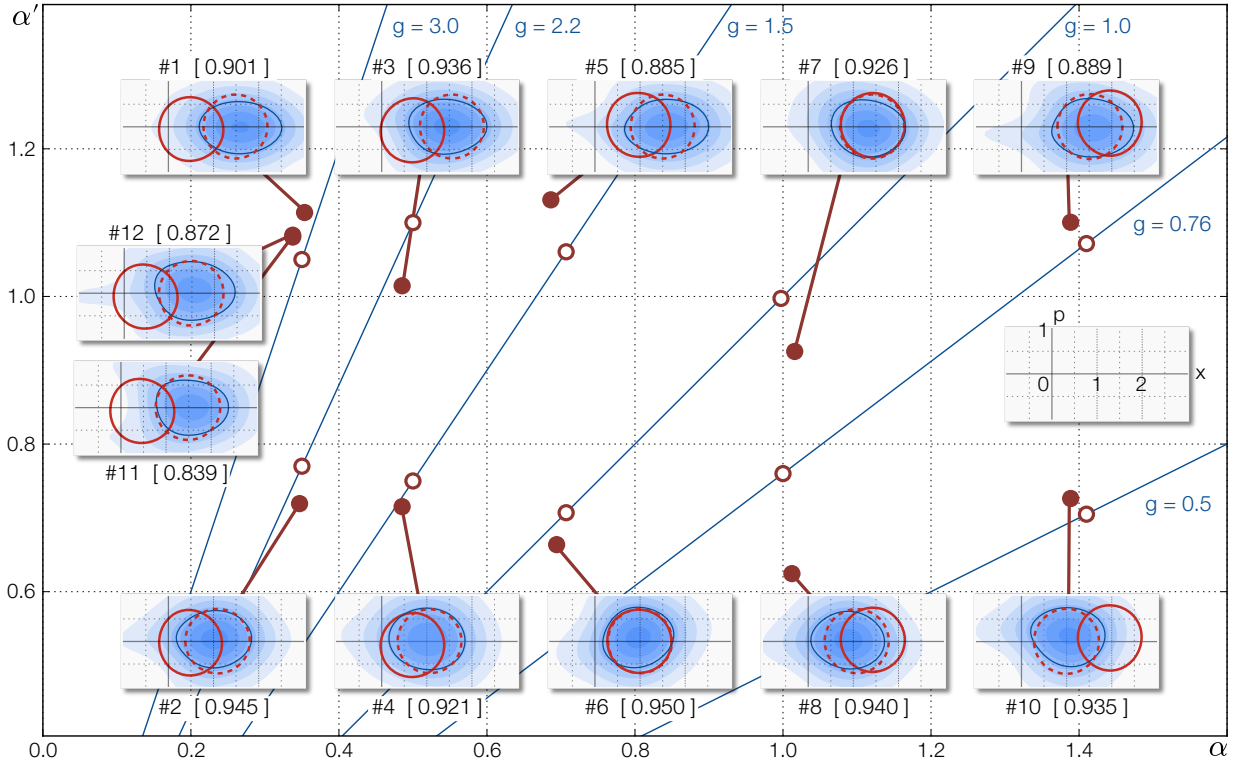


FIG. 2: **Measurement results for the twelve tele-amplifications.** The blue straight lines represent  $\alpha' = g\alpha$ . The open circles represent the sets of  $\alpha$  and  $g_{tg}$  in Table I. The fidelities between the measured states and the targeted  $|g_{tg}\alpha\rangle$  are indicated by the numbers in brackets. Filled circles represent the amplitudes  $\alpha$  ( $\alpha'$ ) of the coherent states that have the maximum fidelity with the measured input (output) states. **Insets:** Output state Wigner functions are shown in blue contour plots. The red solid and dashed circles are for the input and ideal targeted states, respectively.

We carried out an experimental demonstration of the tele-amplification in the simplest case of binary PSK as in Fig. 1b to realize Eq. (6). The resource cat state  $|\Phi_-\rangle$  was generated by photon-subtraction from a squeezed vacuum with anti-squeezing along the real axis in phase space (see Methods). Bob's BS was set to  $R_B = 0.1$ . For a given desired gain  $g$ , we varied  $R_A$  according to Eq. (5). The resource cat-state amplitude  $\beta$ , experimentally tuned by the squeezing level, was then set by Eq. (3). The detector at port C was omitted with negligible effect on the outcomes since the events (A,C)=(1,1) would be rare for our experimental setup. Bob's output state was characterized by homodyne tomography.

We tested in total twelve settings as summarized in Table I. The five different input amplitudes  $\alpha$  were real and ranged between 0.35 and 1.4. The protocol was carried out only for  $|\alpha\rangle$  because the outcome for  $|- \alpha\rangle$  would be trivially identical. The measured results are shown in Fig. 2. The blue straight lines are gain curves  $\alpha' = g\alpha$  in the  $(\alpha, \alpha')$  diagram. The open circles plotted along these lines represent sets of  $\alpha$  and  $g_{tg}$  in Table I. The Wigner functions of the tomographically reconstructed tele-amplified output states  $\hat{\rho}_{out}$  are shown as blue contour plots in the insets. One contour level is highlighted for comparison with the targeted states  $|g_{tg}\alpha\rangle$

(red dashed) and the actual input states  $\hat{\rho}_{in} \approx |\alpha\rangle\langle\alpha|$  (red solid, also characterized by homodyne tomography). The discrepancies between  $\hat{\rho}_{out}$  and  $|g_{tg}\alpha\rangle$  are due to imperfections, including the deviation of the photon-subtracted state from the ideal resource cat, losses, impurity, and Alice's use of an on/off detector instead of two single-photon detectors. For each setting, we calculate which coherent states  $|\alpha\rangle, |\alpha'\rangle$  have the highest fidelity with the measured input and output states, respectively, that is,  $\alpha = \text{argmax}_\gamma \langle\gamma|\hat{\rho}_{in}|\gamma\rangle$  and  $\alpha' = \text{argmax}_{\gamma'} \langle\gamma'|\hat{\rho}_{out}|\gamma'\rangle$ . These  $(\alpha, \alpha')$  pairs are marked as filled circles.

Despite the imperfections, the tele-amplification succeeded with high fidelities  $\langle g_{tg}\alpha|\hat{\rho}_{out}|g_{tg}\alpha\rangle$  between 0.89 and 0.95 as shown next to each inset. The obtained amplitudes (filled circles) are close to the targeted ones (open circles) in almost all cases. The success probabilities were in the range 0.3% to 0.65% (see Methods). For larger  $\alpha'$ , the Wigner function shapes are slightly elongated due to the larger squeezing needed to produce those states. We note that our experimental settings were not fully optimized by taking into account spectral mode mismatch between the resource cat and input coherent states as well as between the APD and homodyne detectors. Had we done it, we estimate the achieved fidelities to have been 0.94–0.99.

#	$\alpha$	$g_{tg}$	$\beta$	$R_A$	$R_E$
1	0.35	3.0	1.11	0.50	0
2	0.35	2.2	0.81	0.65	0
3	0.50	2.2	1.16	0.65	0
4	0.50	1.5	0.79	0.80	0
5	0.71	1.5	1.12	0.80	0
6	0.71	1.0	0.75	0.90	0
7	1.00	1.0	1.05	0.90	0
8	1.00	0.76	0.80	0.94	0
9	1.41	0.76	1.13	0.94	0
10	1.41	0.50	0.74	0.97	0
11	0.35	3.0	1.11	0.50	0.8
12	0.35	3.0	1.11	0.83	0.8

TABLE I: Desired tele-amplification for the twelve settings of input coherent states and gains.  $g_{tg}$  is the targeted gain.

The settings #11 and 12 had an additional 80% loss ( $R_E = 0.8$ ) in the channel from Bob to Alice. In #11,  $R_A = 0.5$  for the original lossless setting (as in #1), while in #12,  $R_A = 0.83$  as optimized according to Eq. (5), resulting in success probabilities of 0.17% and 0.11%. The fidelities with the target state are as high as 0.839 and 0.872, respectively, as compared with 0.901 in the lossless case. This demonstrates the loss tolerance of the protocol.

Teleportation of a cat state qubit as in Eqs. (1–A5) is a prerequisite for CSQC. Interestingly, the tele-amplification allows to convert between different amplitude qubit bases. Although we previously generated such arbitrary cat qubits [17, 23], it was not feasible to tele-amplify them with the current setup since three simultaneous APD clicks would be needed. Instead we simulated this protocol by accurately modelling the current experiment including all relevant practical imperfections (for details, see Appendix F). A cat-state qubit in the Bloch sphere is

$$\begin{aligned} |\psi(\alpha, \theta, \phi)\rangle &= c_+ |\alpha\rangle + c_- |-\alpha\rangle \\ &= \cos\frac{\theta}{2} |\Phi_+(\alpha)\rangle + e^{i\phi} \sin\frac{\theta}{2} |\Phi_-(\alpha)\rangle, \end{aligned}$$

where  $|\Phi_{\pm}(\alpha)\rangle = \mathcal{N}_{\pm}(|\alpha\rangle \pm |-\alpha\rangle)$  are the even/odd cat states with  $\mathcal{N}_{\pm} = 1/\sqrt{2(1 \pm e^{-2\alpha^2})}$  and  $c_{\pm} = \mathcal{N}_{\pm} \cos\frac{\theta}{2} \pm \mathcal{N}_{\mp} e^{i\phi} \sin\frac{\theta}{2}$ .

For a given input state,  $|\psi(\alpha, \theta, \phi)\rangle$ , the model returns an output state  $\hat{\rho}_{\alpha, \theta, \phi}$ , and we calculate the average fidelity of the teleported state with the target state:

$$\mathcal{F}_{\alpha \rightarrow \alpha'}^{\text{avg}} = \int d\phi d\theta \frac{\sin \theta}{4\pi} \langle \psi(\alpha', \theta, \phi) | \hat{\rho}_{\alpha, \theta, \phi} | \psi(\alpha', \theta, \phi) \rangle.$$

In Fig. 3 we plot these average fidelities as a function of input amplitude  $\alpha$  and output amplitudes  $\alpha'$ . We see that for a wide range of parameters it is possible to surpass the classical teleportation limit of 2/3.

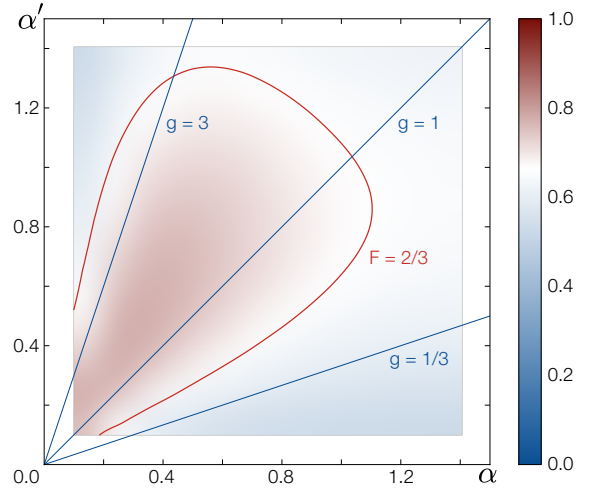


FIG. 3: **Simulated average qubit teleportation fidelity.** Average fidelities as a function of input ( $\alpha$ ) and output state ( $\alpha'$ ) amplitudes for simulated qubit state tele-amplification. The red curve labelled “ $F = 2/3$ ” indicates the classical teleportation bound.

Finally we compare our scheme (Fig. 1a) with the quantum scissor unit used in quantum noiseless amplifiers with single-photon ancilla [27–29]. The schematic difference is only whether the ancilla is a single-photon state or a cat state. The main functional difference is the fidelity to the target state. In the noiseless amplifiers, the fidelity and the success probability rapidly decrease as the amplitude  $\alpha$  increases, because the output state stays in the truncated space spanned by the vacuum and single-photon states. Hence the allowed region for  $\alpha$  is limited for reasonable success rates. Our scheme attains in principle perfect fidelity for arbitrary amplitudes with higher success rates, though at the expense of restricting the input states to finite elements of coherent states.

In summary, we presented tele-amplification of coherent states and a loss-tolerant quantum relay as the first operational application of optical cat states. The scheme is an essential building block for CSQC as well as quantum communications.

## Methods

We generated the squeezed vacua at 860 nm wavelength from an OPO (optical parametric oscillator) continuously pumped with pump parameters between 0.15 and 0.31, corresponding to  $\beta$  values of 0.78 to 1.15. We tapped off 5% of the squeezed beam on a BS and guided it to an APD. A click of the APD heralded the subtraction of a photon from the main beam [14, 23]. The state thus generated is a close approximation to the odd cat state  $|\Phi_-\rangle$ , and has been shown to provide near-perfect teleportation performance [30].

Whenever Alice’s APD clicked simultaneously with the

heralding signal of the single-photon subtraction for the resource cat-state generation, the tele-amplification was successful, and we recorded a trace of the homodyne signal of Bob's output state. The success probability is given by the ratio of the simultaneous click rate ( $\sim 3\text{--}28\text{ s}^{-1}$ ) to the photon subtraction click rate ( $\sim 1000\text{--}4500\text{ s}^{-1}$ ). It is mainly limited by detector and spectral filtering efficiency. To build the homodyne tomogram, we repeated this procedure 6000–24000 times for each fixed input state, with the local oscillator of the homodyne detector locked at phases  $-180^\circ, -150^\circ, \dots, 150^\circ$  with respect to the input state. Note that the protocol succeeds as a single shot for an unknown input state – the repeated measurements with identical inputs are only needed for characterizing the process by homodyne tomography.

Alice's input states were independently characterized by homodyne tomography at port C by setting  $R_A = 1$ . To determine the input states accurately just at Alice's BS, we correct their reconstruction for the detection efficiency and the propagation losses from that point to

the homodyne detector. This total efficiency amounts to 88%. Likewise, in the reconstruction of Bob's output states we correct for the overall detection efficiency of 94% but not for any propagation losses.

A more detailed description of the experimental setup and the state characterization can be found in Appendix E.

## Acknowledgments

We acknowledge helpful discussions with K. Wakui, M. Takeoka, K. Hayasaka, M. Fujiwara, T. Ralph, A. Lund, K. Tamaki, and M. Koashi. This work was partly supported by the FIRST program (Quantum Information Processing Project) and by the National Research Foundation (NRF) grant funded by the Korean Government (MEST) (No. 3348-20100018).

---

[1] Cochrane, P. T., Milburn, G. J. & Munro, W. J. Macroscopically distinct quantum-superposition states as a bosonic code for amplitude damping. *Phys. Rev. A* **59**, 2631–2634 (1999).

[2] Jeong, H. & Kim, M. S. Efficient quantum computation using coherent states. *Phys. Rev. A* **65**, 042305 (2002).

[3] Ralph, T. C., Gilchrist, A., Milburn, G., Munro, W. J. & Glancy, S. Quantum computation with optical coherent states. *Phys. Rev. A* **68**, 042319/1–11 (2003).

[4] Jeong, H. & Ralph, T. C. Schrödinger Cat States for Quantum Information Processing. In N. J. Cerf, G. Leuchs & E. S. Polzik, eds., *Quantum Information with Continuous Variables of Atoms and Light*, chapter 9 (Imperial College Press, London, 2007).

[5] Lund, A. P., Ralph, T. C. & Haselgrove, H. L. Fault-Tolerant Linear Optical Quantum Computing with Small-Amplitude Coherent States. *Phys. Rev. Lett.* **100**, 030503 (2008).

[6] Gerry, C., Benmoussa, A. & Campos, R. Nonlinear interferometer as a resource for maximally entangled photonic states: Application to interferometry. *Phys. Rev. A* **66**, 013804 (2002).

[7] Joo, J., Munro, W. J. & Spiller, T. Quantum Metrology with Entangled Coherent States. *Phys. Rev. Lett.* **107**, 083601 (2011).

[8] Sangouard, N., Simon, C., Gisin, N., Laurat, J., Tualle-Brouri, R. *et al.* Quantum repeaters with entangled coherent states. *J. Opt. Soc. Am. B* **27**, A137 (2010).

[9] Giovannetti, V., Guha, S., Lloyd, S., Maccone, L., Shapiro, J. H. *et al.* Classical Capacity of the Lossy Bosonic Channel: The Exact Solution. *Phys. Rev. Lett.* **92**, 027902 (2004).

[10] Sasaki, M., Sasaki-Usuda, T., Izutsu, M. & Hirota, O. Realization of a collective decoding of code-word states. *Phys. Rev. A* **58**, 159–164 (1998).

[11] Waseda, A., Takeoka, M., Sasaki, M., Fujiwara, M. & Tanaka, H. Quantum detection of wavelength-division-multiplexing optical coherent signals. *J. Opt. Soc. Am. B* **27**, 259 (2010).

[12] Ourjoumtsev, A., Tualle-Brouri, R., Laurat, J. & Grangier, P. Generating optical Schrödinger kittens for quantum information processing. *Science* **312**, 83–86 (2006).

[13] Neergaard-Nielsen, J. S., Nielsen, B. M., Hettich, C., Mølmer, K. & Polzik, E. S. Generation of a Superposition of Odd Photon Number States for Quantum Information Networks. *Phys. Rev. Lett.* **97**, 083604 (2006).

[14] Wakui, K., Takahashi, H., Furusawa, A. & Sasaki, M. Photon subtracted squeezed states generated with periodically poled KTiOPO<sub>4</sub>. *Opt. Express* **15**, 3568–3574 (2007).

[15] Ourjoumtsev, A., Jeong, H., Tualle-Brouri, R. & Grangier, P. Generation of optical 'Schrödinger cats' from photon number states. *Nature* **448**, 784–6 (2007).

[16] Takahashi, H., Wakui, K., Suzuki, S., Takeoka, M., Hayasaka, K. *et al.* Generation of Large-Amplitude Coherent-State Superposition via Ancilla-Assisted Photon Subtraction. *Phys. Rev. Lett.* **101**, 233605 (2008).

[17] Neergaard-Nielsen, J. S., Takeuchi, M., Wakui, K., Takahashi, H., Hayasaka, K. *et al.* Optical Continuous-Variable Qubit. *Phys. Rev. Lett.* **105**, 053602 (2010).

[18] Lee, N., Benichi, H., Takeno, Y., Takeda, S., Webb, J. *et al.* Teleportation of nonclassical wave packets of light. *Science* **332**, 330–3 (2011).

[19] van Enk, S. J. & Hirota, O. Entangled coherent states: Teleportation and decoherence. *Phys. Rev. A* **64**, 022313 (2001).

[20] Jeong, H., Kim, M. & Lee, J. Quantum-information processing for a coherent superposition state via a mixed entangled coherent channel. *Phys. Rev. A* **64**, 052308 (2001).

[21] Jacobs, B., Pittman, T. & Franson, J. Quantum relays and noise suppression using linear optics. *Phys. Rev. A* **66**, 052307 (2002).

[22] Collins, D., Gisin, N. & De Riedmatten, H. Quantum relays for long distance quantum cryptography. *J. Mod. Opt.* **52**, 735–753 (2005).

[23] Takeoka, M., Neergaard-Nielsen, J. S., Takeuchi, M.,

Wakui, K., Takahashi, H. *et al.* Engineering of optical continuous-variable qubits via displaced photon subtraction: multimode analysis. *J. Mod. Opt.* **58**, 266–275 (2011).

[24] Koashi, M. Unconditional Security of Coherent-State Quantum Key Distribution with a Strong Phase-Reference Pulse. *Phys. Rev. Lett.* **93**, 120501 (2004).

[25] Tamaki, K., Lütkenhaus, N., Koashi, M. & Batuwantudawe, J. Unconditional security of the Bennett 1992 quantum-key-distribution scheme with a strong reference pulse. *Phys. Rev. A* **80**, 032302 (2009).

[26] Lo, H.-K. & Preskill, J. Security of quantum key distribution using weak coherent states with nonrandom phases. *Quantum Information and Communication* **7**, 431–458 (2007).

[27] Xiang, G. Y., Ralph, T. C., Lund, A. P., Walk, N. & Pryde, G. J. Heralded noiseless linear amplification and distillation of entanglement. *Nature Photon.* **4**, 316–319 (2010).

[28] Zavatta, A., Fiurášek, J. & Bellini, M. A high-fidelity noiseless amplifier for quantum light states. *Nat. Photonics* **5**, 52–60 (2010).

[29] Ferreyrol, F., Blandino, R., Barbieri, M., Tualle-Brouri, R. & Grangier, P. Experimental realization of a nondeeterministic optical noiseless amplifier. *Phys. Rev. A* **83**, 063801 (2011).

[30] Brańczyk, A. & Ralph, T. C. Teleportation using squeezed single photons. *Phys. Rev. A* **78**, 052304 (2008).

## Appendix A: Tele-amplification of a binary component cat-state

We first describe the tele-amplification of a binary component cat state  $|\psi(\alpha)\rangle_A = c_0 |\alpha\rangle_A + c_1 |-\alpha\rangle_A$

through a lossless channel. The whole three-mode state after the beam-splitting operation in Fig. 1a is given by

$$\begin{aligned}
|\Psi\rangle_{ABC} &= \hat{V}_{AC} |\psi(\alpha)\rangle_A \hat{V}_{BC} |\Phi\rangle_B |0\rangle_C \\
&= \mathcal{N} c_0 \left| \sqrt{1-R_A} \alpha - \sqrt{R_A R_B} \beta \right\rangle_A \left| \sqrt{1-R_B} \beta \right\rangle_B \left| -\sqrt{R_A} \alpha - \sqrt{(1-R_A) R_B} \beta \right\rangle_C \\
&\quad - \mathcal{N} c_0 \left| \sqrt{1-R_A} \alpha + \sqrt{R_A R_B} \beta \right\rangle_A \left| -\sqrt{1-R_B} \beta \right\rangle_B \left| -\sqrt{R_A} \alpha + \sqrt{(1-R_A) R_B} \beta \right\rangle_C \\
&\quad + \mathcal{N} c_1 \left| -\sqrt{1-R_A} \alpha - \sqrt{R_A R_B} \beta \right\rangle_A \left| \sqrt{1-R_B} \beta \right\rangle_B \left| \sqrt{R_A} \alpha - \sqrt{(1-R_A) R_B} \beta \right\rangle_C \\
&\quad - \mathcal{N} c_1 \left| -\sqrt{1-R_A} \alpha + \sqrt{R_A R_B} \beta \right\rangle_A \left| -\sqrt{1-R_B} \beta \right\rangle_B \left| \sqrt{R_A} \alpha + \sqrt{(1-R_A) R_B} \beta \right\rangle_C
\end{aligned} \tag{A1}$$

where  $\mathcal{N} = 1/\sqrt{2[1 - \exp(-2|\beta|^2)]}$  is the normalization of the resource cat state  $|\Phi\rangle_B$ . We now impose a condition on the amplitude of the resource cat-state

$$\beta = \sqrt{\frac{1-R_A}{R_A R_B}} \alpha \tag{A2}$$

such that the components at port A turn into either of the vacuum or non-vacuum states as

$$\begin{aligned}
|\Psi\rangle_{ABC} &= \mathcal{N} c_0 |0\rangle_A |g\alpha\rangle_B \left| -\frac{1}{\sqrt{R_A}} \alpha \right\rangle_C \\
&\quad - \mathcal{N} c_0 \left| 2\sqrt{1-R_A} \alpha \right\rangle_A | -g\alpha \rangle_B \left| \frac{1-2R_A}{\sqrt{R_A}} \alpha \right\rangle_C \\
&\quad + \mathcal{N} c_1 \left| -2\sqrt{1-R_A} \alpha \right\rangle_A | g\alpha \rangle_B \left| -\frac{1-2R_A}{\sqrt{R_A}} \alpha \right\rangle_C \\
&\quad - \mathcal{N} c_1 |0\rangle_A | -g\alpha \rangle_B \left| \frac{1}{\sqrt{R_A}} \alpha \right\rangle_C
\end{aligned} \tag{A3}$$

with the gain

$$g = \sqrt{(1-R_A)(1-R_B)/R_A R_B} \tag{A4}$$

Alice then performs single photon detection on paths A and C as shown in Fig. 1a, and selects single photon at port A and nothing at port C – denoted (1,0). Then Bob can unambiguously exclude the first and fourth terms in Eq. (A3), and has the state

$$_{AC} \langle 1, 0 | \Psi \rangle_{ABC} \propto |\psi(-g\alpha)\rangle_B. \tag{A5}$$

In the case where the channel between Alice and Bob is subject to a linear loss with the rate  $R_E$ , one can consider an external mode E. Bob chooses the cat-state amplitude as

$$\beta = \sqrt{\frac{1-R_A}{R_A R_B (1-R_E)}} \alpha. \tag{A6}$$

The whole state before Alice's measurement is

$$\begin{aligned}
|\Psi\rangle_{ABCE} &= \hat{V}_{AC} |\psi\rangle_A \hat{V}_{EC} \hat{V}_{BC} |\Phi\rangle_B |0\rangle_C |0\rangle_E \\
&= \mathcal{N} c_0 |0\rangle_A |g\alpha\rangle_B \left| -\frac{1}{\sqrt{R_A}} \alpha \right\rangle_C | -\varepsilon \rangle_E \\
&\quad - \mathcal{N} c_0 \left| 2\sqrt{1-R_A} \alpha \right\rangle_A | -g\alpha \rangle_B \left| \frac{1-2R_A}{\sqrt{R_A}} \alpha \right\rangle_C | \varepsilon \rangle_E \\
&\quad + \mathcal{N} c_1 \left| -2\sqrt{1-R_A} \alpha \right\rangle_A | g\alpha \rangle_B \left| -\frac{1-2R_A}{\sqrt{R_A}} \alpha \right\rangle_C | -\varepsilon \rangle_E \\
&\quad - \mathcal{N} c_1 |0\rangle_A | -g\alpha \rangle_B \left| \frac{1}{\sqrt{R_A}} \alpha \right\rangle_C | \varepsilon \rangle_E
\end{aligned} \tag{A7}$$

with the gain

$$g = \sqrt{\frac{(1-R_A)(1-R_B)}{R_A R_B (1-R_E)}} \tag{A8}$$

and  $\varepsilon = \sqrt{(1-R_A)R_E/R_A(1-R_E)}\alpha$ .

## Appendix B: Extension to multi-ary coherent states

The binary case can be extended to  $M$ -ary phase-shift-keyed coherent states  $|\alpha_m\rangle$ , where

$$\alpha_m = \alpha u^m, \quad u = e^{2\pi i/M}. \tag{B1}$$

Here  $\alpha_0 = \alpha$  is taken to be real. The states are generated by

$$|\alpha_m\rangle = \hat{V}^m |\alpha_0\rangle, \quad \hat{V} = \exp\left(\frac{2\pi i}{M} \hat{n}\right). \tag{B2}$$

An input state at Alice is

$$|\psi\rangle_A = \sum_{m=0}^{M-1} c_m |\alpha_m\rangle_A. \tag{B3}$$

Bob prepares a cat state for the entanglement resource,

$$|\Phi\rangle_B = \sum_{k=0}^{M-1} b_k |\beta_k\rangle_B. \quad (\text{B4})$$

In order to see what kind of cat state is appropriate, we introduce the orthonormal basis  $\{|\omega_m\rangle\}$ , which diagonalize the generating operator as

$$\hat{V} = \sum_{k=0}^{M-1} u^k |\omega_k\rangle \langle \omega_k|. \quad (\text{B5})$$

Then

$$|\beta_m\rangle = \sum_{m=0}^{M-1} u^{mk} |\omega_k\rangle \langle \omega_k| \beta. \quad (\text{B6})$$

Using the orthogonality property

$$\sum_{k=0}^{M-1} u^{(m-n)k} = M\delta_{m,n}, \quad (\text{B7})$$

we have

$$|\omega_m\rangle = \frac{1}{M} \langle \omega_m | \beta \rangle \sum_{k=0}^{M-1} u^{-mk} |\beta_k\rangle. \quad (\text{B8})$$

The normalization condition  $\langle \omega_m | \omega_m \rangle = 1$  means

$$|\langle \omega_m | \beta \rangle|^2 = \frac{1}{M^2} \sum_{k'=0}^{M-1} \sum_{k=0}^{M-1} u^{(k'-k)m} \langle \beta_{k'} | \beta_k \rangle. \quad (\text{B9})$$

Because the matrix  $(\langle \beta_{k'} | \beta_k \rangle)$  is cyclic,

$$|\langle \omega_m | \beta \rangle|^2 = \frac{1}{M} \sum_{k=0}^{M-1} u^{-km} \langle \beta_0 | \beta_k \rangle. \quad (\text{B10})$$

Define a quantity

$$\lambda_m = M |\langle \omega_m | \beta \rangle|^2. \quad (\text{B11})$$

Then one can see

$$\hat{\rho} = \sum_{m=0}^{M-1} |\beta_m\rangle \langle \beta_m| = \sum_{m=0}^{M-1} \lambda_m |\omega_m\rangle \langle \omega_m|. \quad (\text{B12})$$

These eigenvalues are related to the mean photon number of the basis states as

$$\langle \omega_m | \hat{n} | \omega_m \rangle = \frac{|\beta|^2}{\lambda_m}. \quad (\text{B13})$$

To maximize the success probability of Alice's measurement, one should use the  $|\omega_m\rangle$  which has the maximum photon number, namely the minimum eigenvalue, for the entanglement resource. For relatively smaller  $|\beta|$ , it is the  $|\omega_{M-1}\rangle$ .

Now let us see the case of  $M = 4$  ( $u = i$ ). The cat state for the entanglement resource is

$$|\Phi\rangle_B = |\omega_3\rangle_B = \frac{1}{\sqrt{4\lambda_3}} \sum_{k=0}^{M-1} u^k |\beta_k\rangle_B. \quad (\text{B14})$$

The eigenvalues are given by

$$\begin{aligned} \lambda_0 &= 2e^{-\beta^2} (\cosh \beta^2 + \cos \beta^2), \\ \lambda_1 &= 2e^{-\beta^2} (\sinh \beta^2 + \sin \beta^2), \\ \lambda_2 &= 2e^{-\beta^2} (\cosh \beta^2 - \cos \beta^2), \\ \lambda_3 &= 2e^{-\beta^2} (\sinh \beta^2 - \sin \beta^2). \end{aligned} \quad (\text{B15})$$

The above state is beam-split into paths B and C, the component of mode C is sent to Alice through a lossy channel, and then combined with the input at path A.

Bob chooses the cat-state amplitude as Eq. (A6). The whole state before the measurement is given by

$$\begin{aligned} |\Psi\rangle_{BACE} &= \sum_{m=0}^3 c_m \sum_{k=0}^3 \frac{u^k}{\sqrt{4\lambda_3}} |g\alpha u^k\rangle_B \\ &\otimes \left| \sqrt{1-R_A} \alpha (u^m - u^k) \right\rangle_A \\ &\otimes \left| -\frac{\alpha}{\sqrt{R_A}} [R_A u^m + (1-R_A) u^k] \right\rangle_C \\ &\otimes |\varepsilon u^k\rangle_E \end{aligned} \quad (\text{B16})$$

with the gain given by Eq. (A8).

We set  $R_A = 0.5$ . Alice further introduces additional modes A' and C' to implement the four-port single photon detection as shown in Fig. 1b. The state before the detection is given by

$$\begin{aligned} |\Psi\rangle_{BAA'CC'E} &= \sum_{m=0}^3 c_m \sum_{k=0}^3 u^k |g\alpha u^k\rangle_B \\ &\otimes \left| \alpha \frac{u^m - u^k}{2} \right\rangle_A \\ &\otimes \left| -\alpha \frac{u^m + u^k}{2} \right\rangle_C \\ &\otimes \left| \alpha \frac{u^m - u^{m+1} + u^k + u^{k+1}}{2\sqrt{2}} \right\rangle_{A'} \\ &\otimes \left| \alpha \frac{u^m + u^{m+1} + u^k - u^{k+1}}{2\sqrt{2}} \right\rangle_{C'} \\ &\otimes \left| \frac{R_E}{\sqrt{1-R_E}} \alpha u^k \right\rangle_E \end{aligned} \quad (\text{B17})$$

When the loss can be neglected ( $R_E = 0$ ), the input  $|\psi\rangle$  of Eq. (B18) can be faithfully tele-amplified to the target state

$$|g\psi\rangle_B = \sum_{m=0}^{M-1} c_m |g\alpha_m\rangle_B, \quad (\text{B18})$$

by selecting a set of Alice's measurement result as (A, A', C, C')=(0,1,1,1), namely no count at port A while single photon counts at port A', C, and C'.

In the lossy case, it is impossible to teleport a superposition state faithfully. However, when an input is restricted to a classical state drawn from the set  $|\alpha_m\rangle$ , then the tele-amplification to the target pure state is possible. Actually depending on a set of the results at the four ports, (A, A', C, C'), the inputs are tele-amplified as

$$\begin{aligned} |\alpha_m\rangle &\mapsto |g\alpha_m\rangle, & \text{for } (0, 1, 1, 1), \\ |\alpha_m\rangle &\mapsto |ig\alpha_m\rangle, & \text{for } (1, 0, 1, 1), \\ |\alpha_m\rangle &\mapsto |-g\alpha_m\rangle, & \text{for } (1, 1, 0, 1), \\ |\alpha_m\rangle &\mapsto |-ig\alpha_m\rangle, & \text{for } (1, 1, 1, 0). \end{aligned} \quad (\text{B19})$$

### Appendix C: On/off detection at Alice

In our experiment, Alice's measurement is implemented by avalanche photo diodes (APDs) instead of ideal "single photon detectors" that discriminate between "0", "1" and "2 or more" photons. APDs cannot, however, discriminate photon numbers, but distinguish merely the vacuum or non-vacuum state, i.e. "off" or "on". They are represented by the operators

$\hat{\Pi}_{\text{off}} = |0\rangle\langle 0|$  and  $\hat{\Pi}_{\text{on}} = \hat{I} - |0\rangle\langle 0|$ . Then the tele-amplification described in the previous section should be corrected slightly. For example, Eq. (A5) for the binary case becomes

$$\begin{aligned} ABC\langle\Psi|\hat{\Pi}_{\text{on}}^A\hat{\Pi}_{\text{off}}^C|\Psi\rangle_{ABC} &= |\psi(-g\alpha)\rangle_B\langle\psi(-g\alpha)| \\ &+ \tanh\left(\frac{\tilde{\alpha}}{2}\right)|\tilde{\psi}(-g\alpha)\rangle_B\langle\tilde{\psi}(-g\alpha)| \end{aligned} \quad (\text{C1})$$

where  $|\tilde{\psi}(-g\alpha)\rangle = c_0|\alpha\rangle - c_1|-\alpha\rangle$  and  $\tilde{\alpha} = 2\sqrt{1-R_A}\alpha$ . The second term is the correction. When  $\alpha$  is small, the coefficient of the second term is small as  $\tanh(\tilde{\alpha}/2) \sim \tilde{\alpha}/2$ . In this regime, the tele-amplification would approximately work with on/off detection. However, in general, the second term cannot be ignored.

If the input state was a coherent state, i.e.,  $c_0 = 0$  or  $c_1 = 0$ , the above state would become a pure coherent state with the gain  $g$ , and on/off detection would be sufficient.

### Appendix D: Success probability

#### 1. Loss tolerant quantum relay

In the binary case, the input is either of  $|\alpha\rangle$  and  $|-\alpha\rangle$ . The whole state before Alice's measurement is

$$\begin{aligned} |\Psi_{\pm}\rangle &= \hat{V}_{AC}|\pm\alpha\rangle_A\hat{V}_{EC}\hat{V}_{BC}|\Phi\rangle_B|0\rangle_C|0\rangle_E \\ &= \pm\mathcal{N}|0\rangle_A|\pm g\alpha\rangle_B\left|\mp\frac{1}{\sqrt{R_A}}\alpha\right\rangle_C|\mp\alpha'\rangle_E\mp\mathcal{N}\left|\pm 2\sqrt{1-R_A}\alpha\right\rangle_A|\mp g\alpha\rangle_B\left|\pm\frac{1-2R_A}{\sqrt{R_A}}\alpha\right\rangle_C|\pm\alpha'\rangle_E \end{aligned} \quad (\text{D1})$$

The success probability of the tele-amplification  $|\pm\alpha\rangle_A \mapsto |\pm g\alpha\rangle_B$  is given by the expectation value of  $\hat{\Pi}_{10} \equiv \hat{\Pi}_{\text{on}}^A \otimes \hat{\Pi}_{\text{off}}^C$  as

$$\begin{aligned} P_{\text{Tele-amp}}^{(2)} &= \frac{1}{2}\langle\Psi_+|\hat{\Pi}_{10}|\Psi_+\rangle + \frac{1}{2}\langle\Psi_-|\hat{\Pi}_{10}|\Psi_-\rangle \\ &= \frac{\exp\left[-\frac{(1-2R_A)^2}{R_A}\alpha^2\right] - \exp\left[-\frac{\alpha^2}{R_A}\right]}{2\left(1 - \exp\left[-\frac{2(1-R_A)}{R_A R_B(1-R_E)}\alpha^2\right]\right)}. \end{aligned} \quad (\text{D2})$$

In the case of 4-PSK states, the state before Alice's measurement is given by

$$\begin{aligned} |\Psi_m\rangle &= \sum_{k=0}^3 u^k |g\alpha u^k\rangle_B \\ &\otimes \left|\alpha\frac{u^m - u^k}{2}\right\rangle_A \left|-\alpha\frac{u^m + u^k}{2}\right\rangle_C \\ &\otimes \left|\alpha\frac{u^m - u^{m+1} + u^k + u^{k+1}}{2\sqrt{2}}\right\rangle_{A'} \\ &\otimes \left|\alpha\frac{u^m + u^{m+1} + u^k - u^{k+1}}{2\sqrt{2}}\right\rangle_{C'} \\ &\otimes \left|\frac{R_E}{\sqrt{1-R_E}}\alpha u^k\right\rangle_E \end{aligned} \quad (\text{D3})$$

The success probability of  $|\alpha_m\rangle_A \mapsto |g\alpha_m\rangle_B$  is given by the expectation value of

$$\hat{\Pi}_{0111} \equiv \hat{\Pi}_{\text{off}}^A \otimes \hat{\Pi}_{\text{on}}^{A'} \otimes \hat{\Pi}_{\text{on}}^C \otimes \hat{\Pi}_{\text{on}}^{C'} \quad (\text{D4})$$

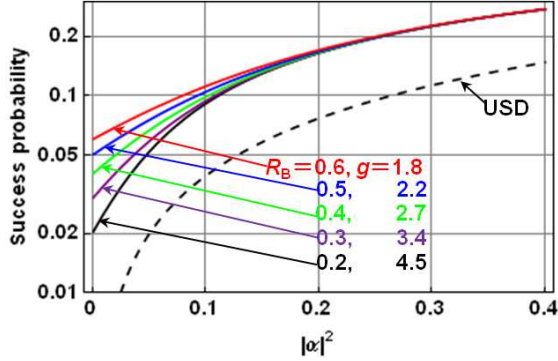


FIG. 4: Success probabilities for the case of the BPSK coherent states. The solid lines are for the quantum relay with several cases of the amplification gains, while the dashed line is for the measure-resend strategy with the unambiguous state discrimination.

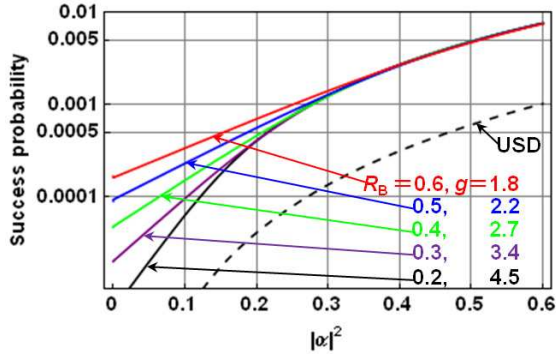


FIG. 5: Success probabilities for the case of the 4PSK coherent states.

as

$$\begin{aligned} P_{Tele-amp}^{(4)} &= \frac{1}{4} \sum_{k=0}^3 \langle \Psi_m | \hat{\Pi}_{0111} | \Psi_m \rangle \\ &= \langle \Psi_0 | \hat{\Pi}_{0111} | \Psi_0 \rangle \\ &= \frac{(1 - e^{-\alpha^2/2})^2 (1 - e^{-\alpha^2})}{4 \lambda_3(\frac{\alpha^2}{R_B(1-R_E)})} \end{aligned} \quad (D5)$$

where

$$\lambda_3(x) = 2e^{-x}(\sinh x - \sin x). \quad (D6)$$

## 2. Measure-resend strategy

The task to relay attenuated coherent states to the receiver, converting them faithfully to the target amplified states, can also be realized by a classical strategy. A typical one is a measure-resend strategy. In the intermediate node, Bob has attenuated states  $\{|\sqrt{1-R_E}\alpha_m\rangle\}$ .

He tries to discriminate them unambiguously without errors, but at a finite success rate, and then prepare a target amplified state  $|g\sqrt{1-R_E}\alpha_m\rangle$  for the measurement result  $m$ . The success rate is well known for this kind of equally probable symmetric states [1]. Denoting  $|\gamma_m\rangle = |\sqrt{1-R_E}\alpha_m\rangle$  and using the eigenvalues and the diagonalizing vectors of the density operator

$$\hat{\rho} = \sum_{m=0}^{M-1} |\gamma_m\rangle \langle \gamma_m| = \sum_{m=0}^{M-1} \lambda_m |\omega_m\rangle \langle \omega_m|, \quad (D7)$$

the success rate is given by

$$P_{USD} = \min_k \lambda_k. \quad (D8)$$

The signal states are represented as

$$\begin{aligned} |\gamma_m\rangle &= \left| \sqrt{1-R_E}\alpha_m \right\rangle \\ &= \frac{1}{\sqrt{M}} \sum_{k=0}^{M-1} \sqrt{\lambda_k} u^{mk} |\omega_k\rangle. \end{aligned} \quad (D9)$$

The detection operators are given by

$$\hat{\Pi}_m = \frac{\Lambda}{M} P_{USD} |\gamma_m^\perp\rangle \langle \gamma_m^\perp| \quad (D10)$$

for the signal state  $|\gamma_m\rangle$ , using the reciprocal states

$$|\gamma_m^\perp\rangle = \frac{1}{\sqrt{\Lambda}} \sum_{k=0}^{M-1} \frac{u^{mk}}{\sqrt{\lambda_k}} |\omega_k\rangle \quad (D11)$$

where  $\Lambda = \sum_k \lambda_k^{-1}$ . They satisfy the orthogonality relation

$$\langle \gamma_m^\perp | \gamma_{m'} \rangle = \sqrt{\frac{M}{\Lambda}} \delta_{m,m'}. \quad (D12)$$

The operator for the inconclusive result is given by

$$\hat{\Pi}_F = \hat{I} - \sum_{m=0}^{M-1} \hat{\Pi}_m. \quad (D13)$$

## 3. Numerical results for BPSK coherent states

The success probabilities are shown in Fig. 4 for the BPSK coherent states, and in Fig. 5 for the 4PSK coherent states, in comparison with that by the measure-resend strategy. The quantum relay can attain higher success rates than that by the above measure-resend strategy. In the case of 4PSK states, the difference is as high as ten times.

## Appendix E: Experimental details

### 1. Setup

The most relevant elements of the experimental setup are sketched in Fig. 6 and described in the following.

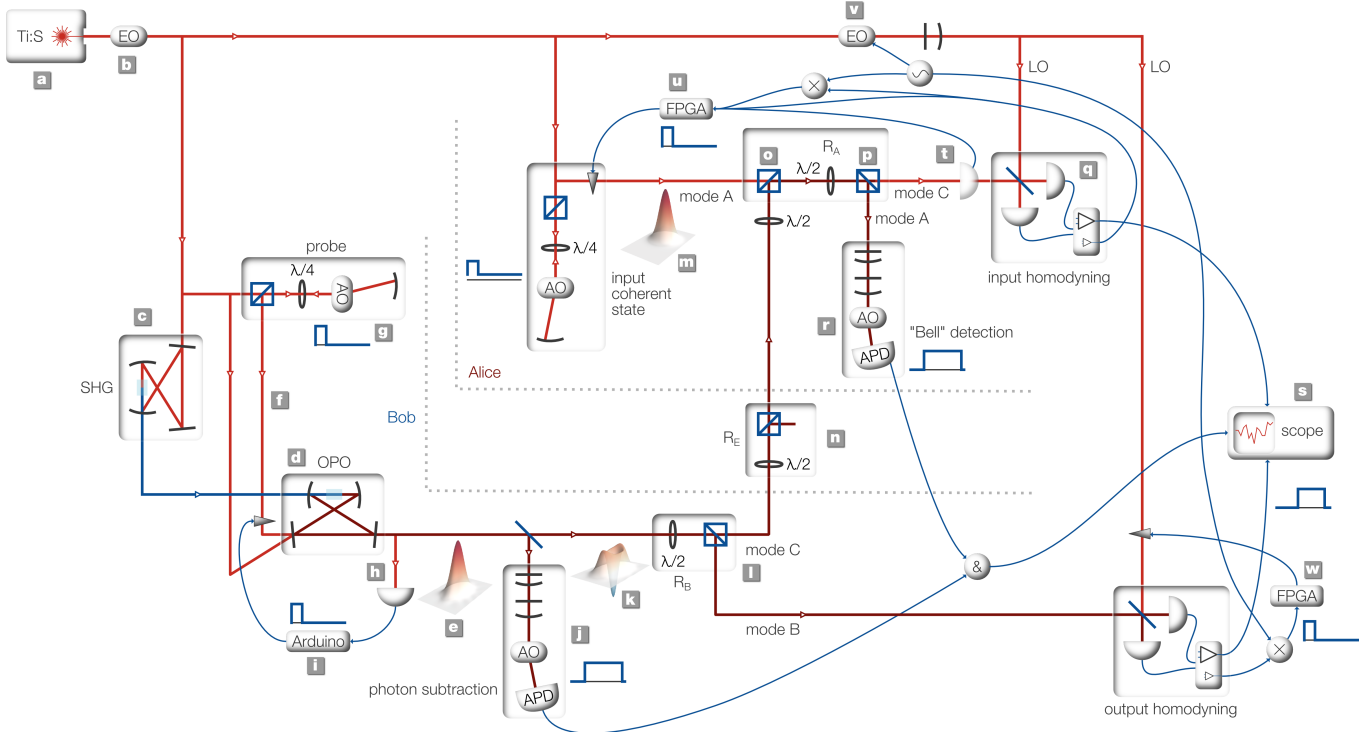


FIG. 6: Sketch of the experimental setup for tele-amplification of a coherent state from Alice to Bob using shared entanglement in the form of a photon-subtracted squeezed vacuum state.

#### Resource state generation

The output of an 860 nm continuous-wave Ti:Sapph laser (a) is phase-modulated by an EOM (b) for Pound-Drever locking of the SHG and OPO cavities. Parts of the beam are tapped off for use as local oscillators, coherent input beam, probe beam and cavity locking beams, but the main part is frequency-doubled in the second harmonic generator (c). The 430 nm output of this SHG pumps a bow-tie configuration optical parametric oscillator (OPO, d) with a PPKTP crystal and a HWHM bandwidth of  $\gamma/2\pi = 4.5$  MHz. The down-converted light leaving the cavity is in a squeezed vacuum state (e). A probe beam (f) is injected into the OPO for the purpose of locking phases and filtering cavities further downstream.

The whole experiment is running in an alternating lock/measure cycle at a rate of 10 kHz. The probe beam is thus switched on and off by double-passes through two acousto-optical modulators (only one shown in the figure) that are driven for only 20% of the 10 kHz cycle time, as indicated by the blue pulse diagram (g) (this diagram is repeated for other relevant parts of the setup).

In order to act as a phase-reference for the squeezing, the probe beam is locked in phase with the squeezed quadrature by observing its classical parametric amplification in the OPO through a <1% tap-off of the OPO output (h). To obtain an error-signal, the probe's

phase is dithered on a piezo-mounted mirror by a micro-controller unit (Arduino) which also processes the detected signal and provides feedback to lock the phase (i).

A photon is subtracted from the squeezed vacuum at random times by the detection on an avalanche photodiode (APD) detector, placed after a 5% tapping beam-splitter and two frequency-filtering cavities (j). The APD is protected from the strong probe beam by an AOM that directs the OPO output to the APD only during the intervals when the probe beam is switched off. The resulting photon-subtracted squeezed vacuum (PSSV) state (k) is the resource of entanglement in our protocol, after it is split into two modes propagating towards the Alice and Bob sections of the setup. In the description of the protocol in the main section, a fraction  $R_B = 0.1$  is reflected towards Alice. In the actual experiment (and in the setup sketch), Alice's fraction  $R_B$  is actually taken as the transmitted part of a variable beam-splitter fixed at 90% reflection (l). Bob's share of the entangled state is directed towards a homodyne detector for output state analysis.

The amount of squeezing produced by the OPO determines the amplitude of the cat-like PSSV state. It is regulated by the pump parameter  $\epsilon = \sqrt{P_{\text{pump}}/P_{\text{threshold}}}$ . To find what cat amplitude  $\beta$  a given pump parameter corresponds to, we model the PSSV as in Ref. [23] of the main text. Here, we include the OPO temporal correlations, the temporal modes of the APD and homodyne detection (described in the following section), the

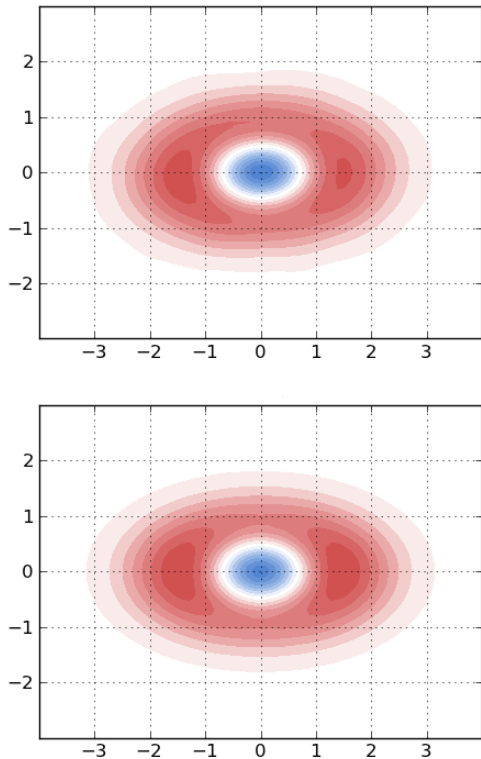


FIG. 7: Wigner function for one of the PSSV states used as approximations for the odd cat resource state, in this case with  $\epsilon = 0.20$ . The upper is experimentally generated and tomographically reconstructed, while the lower one is obtained from our model. The fidelity between them is above 98%, showing the validity of the model.

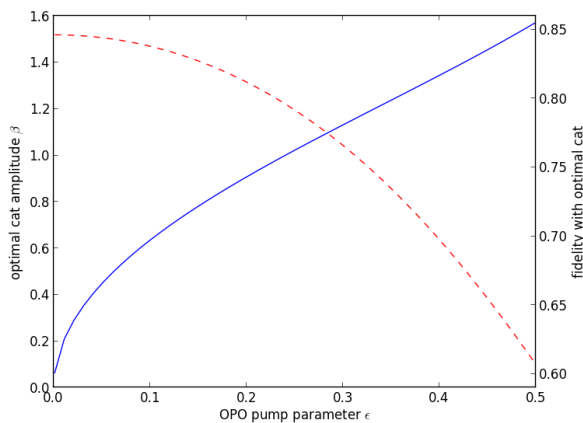


FIG. 8: Relation between OPO pump parameter  $\epsilon$  for the production of realistic PSSV states and the amplitude of the cat state  $|\Phi_-(\beta)\rangle$  that maximizes the mutual fidelity. The blue curve indicates these optimal  $\beta$  amplitudes, while the dashed red curve shows the corresponding fidelities. In the experiment, we used  $\epsilon$  in the range 0.15–0.31.

96% escape efficiency of the OPO, the 95% propagation efficiency towards the beam-splitter (l), the 5% tapping ratio, the  $\sim 10\%$  overall APD detection efficiency, and the filtering bandwidth to find a  $\hat{\rho}_{\text{PSSV}}$  that closely emulates the actually produced states. Fig. 7 shows an example of an experimentally generated PSSV state and, for comparison, the modelled state with equivalent parameters. We then maximize for  $\beta$  the state's fidelity with a true cat state,  $\langle \Phi_-(\beta) | \hat{\rho}_{\text{PSSV}} | \Phi_-(\beta) \rangle$ , and get the  $\epsilon \rightarrow \beta$  correspondence plotted in Fig. 8 and thereby the  $\beta$  values of Table I.

#### Input state and teleportation

Alice's input coherent state (m) is prepared in a configuration of two double-pass AOMs similar to that used for the OPO probe beam, with a strong phase locking beam switched on during the 20% locking part of the 10 kHz cycle. However, instead of switching the light completely off during the remaining 80% of the cycle, a weak amplitude beam is generated instead. This is done by switching to a lower voltage RF driving signal for the AOM.

The share of the entangled PSSV state propagating from Bob to Alice in mode C is optionally subjected to a loss at a variable beam-splitter (n) before it is overlapped with her input state on a polarizing beam splitter (PBS) in orthogonal polarizations (o). A half-waveplate followed by another PBS (p) then interferes the two modes as the protocol's  $R_A$  reflectivity beam-splitter. When characterizing the input state,  $R_A$  is set to 1, which means that all of the input state is sent towards the homodyne detector (q). Otherwise, when running the tele-amplification protocol,  $R_A$  is set to its appropriate value, and the output of the beamsplitter in mode A is sent towards an APD (r) with the same frequency filtering and chopping configuration as that in (j).

The detection events from the two APDs are correlated with digital timing electronics that pick out simultaneous events and triggers the acquisition of Bob's homodyne signal at a fast digital oscilloscope (s). The detected photo-currents are subsequently temporally filtered on a PC to extract the measured quadrature values, as described in the following section.

#### Phase locking

For the tele-amplification protocol to work, the input states  $|\pm\alpha\rangle$  should be interfered in-phase with the anti-squeezed quadrature of the entangled PSSV state. We do this by putting a normal intensity detector (t) at the mode C output port of the beamsplitter instead of Alice's homodyne detector (q). The detected interference signal between the probe portions of the input coherent state beam and the PSSV state beam is used as the input to an FPGA-based lock unit, which provides feedback to the phase of the input beam (u). When the two beams are

interfered at  $90^\circ$ , we get the desired phase relation, since the PSSV probe was locked to the squeezed quadrature.

The phase of the local oscillators (LO) in the two homodyne detectors can be locked to arbitrary phases relative to the PSSV probe by using a combination of DC and side-band detection of the interference between the LO and the probe beam. An 8 MHz phase modulation is applied to the LO (v), and the interference signals observed by the fast homodyne detectors (from a separate low-gain amplification output) are demodulated at that same frequency. This provides an interference signal that is  $90^\circ$  out of phase with the DC signal. In the FPGA lock units (u,w), the two signals are added with weighting factors corresponding to the desired LO phase in phase space, resulting in an error signal for the feedback to piezo-mounted mirrors in the LO beam path (in the case of Bob's output homodyner) or in the input beam path (for Alice).

All phase locks are engaged only during the intervals of the 10 kHz experiment cycle in which the probe beams are turned on. For the remaining, the feedback signals are just held at their last actively set value.

## 2. Quantum state tomography

### Temporal modes

The squeezed vacuum has a bandwidth given by the OPO's HWHM of  $\gamma/2\pi = 4.5$  MHz. Conditioned on an APD click at time  $t_0$ , the continuous-wave squeezed vacuum is converted into a temporally localized PSSV state in a temporal mode around  $t_0$  which, in the low-squeezing limit, has the form  $\exp(-\gamma|t - t_0|)$  [2]. The filter cavities in front of the APD, needed to remove the photons down-converted into the many non-degenerate OPO resonances, modify the temporal mode to be

$$f(t) \propto \gamma^{-1} e^{-\gamma|t-t_0|} - \kappa^{-1} e^{-\kappa|t-t_0|}, \quad (E1)$$

where  $\kappa/2\pi \approx 25$  MHz is the combined bandwidth of the two filters, approximated by a single Lorentzian spectral profile. This will also be the temporal mode of the teleported output state in the low-squeezing limit. For the state tomography, we therefore extract a single quadrature value from the continuous photo current signal of the homodyne detector by integrating it over a mode  $f_{\text{HD,out}}(t)$  equal to the one in Eq. (E1). At higher squeezing levels, the optimal mode function is not that simple [3], but in this work we stick to the simple expression for all squeezing levels.

An interesting, but also complicating aspect of our current implementation of the tele-amplification protocol is that the input and output states are in rather different spectral modes: The input coherent state is derived directly from the narrow-band laser, whereas the entangled PSSV state is in the broadband mode described above. At a first glance it would appear like the two modes will

not interfere well and the teleportation will fail. However, the spectral response of Alice's APD is very broad, so it is unable to distinguish the modes. Thereby it can be said that the detection itself induces the interference between the input and the entangled state. Another way to see it is in the time domain: compared to the cw input beam and the  $\sim 1/\gamma$  extent of the PSSV state, the temporal response of the APD ( $\sim 350$  ps jitter) is essentially delta function-like. Within this short time window, almost no phase shift will occur between the different frequency components, so interference will not be destroyed.

One problem we do get from this spectral mismatch, however, is the issue of which temporal mode,  $f_{\text{HD,in}}(t)$  to use for the definition of the coherent input state. As the beam is continuous, the choice of temporal mode can be done arbitrarily. The photon number  $n_{\text{in}}$  within the chosen mode will be proportional to the width of the mode function, so to obtain a desired coherent state the intensity of the beam should be adjusted inversely proportional to that width. In our experiment we make the rather natural choice to use the  $f_{\text{HD,out}}(t)$  mode, such that we observe the same temporal mode in both the input and the output homodyne tomography. The measured  $\alpha$  and  $\alpha'$  values in Fig. 2 are therefore directly comparable.

However, this mode is not the one detected by the APD. Since the APD with its delta function-like response is preceded by filtering cavities which act as delays for incoming fields, its temporal mode can be approximately described as a single-sided exponential decay, with time constant given by the filter bandwidth,

$$f_{\text{APD}}(t) \propto e^{-\kappa|t-t_0|} H(t_0 - t), \quad (E2)$$

with  $H(t)$  being the Heaviside step function. Because the PSSV entangled state is temporally localized, as opposed to the input state, the ratio of the photon numbers of the two states,  $n_{\text{in}}/n_{\text{PSSV}}$  will be different within the different modes  $f_{\text{HD,in}}(t)$  and  $f_{\text{APD}}(t)$ . There is therefore a mismatch between the input state amplitude,  $\alpha$ , that we expect to have and the amplitude actually seen by Alice's APD, which is the one to induce the teleportation. Thus, the  $\beta$  and  $R_A$  values that we experimentally adjusted to match a given  $\alpha$  were actually not optimal, and this resulted in output-to-target fidelities that were lower than we could have otherwise obtained. In a possible follow-up experiment, it would be advisable to consider this issue of the input state amplitude in more detail. Simulations indicate that with optimized settings, fidelities could have reached 0.94–0.99.

### State reconstruction

For a given realization of the tele-amplification, we construct a homodyne tomogram of the output (and input) state by repeating the state preparation, on/off detection and conditional homodyne detection multiple times, with the LO phase of the homodyne detector fixed at

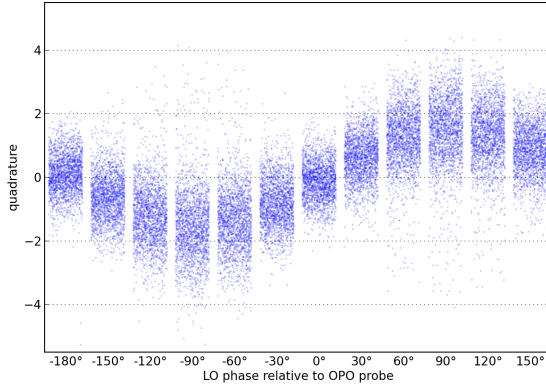


FIG. 9: Example tomogram, showing the  $12 \times 2000$  quadrature values of the homodyne measurement of the output state in tele-amplification #5.

various angles. After filtering the oscilloscope traces with the chosen temporal mode, as described above, the obtained quadrature values are normalized by vacuum traces recorded under the same experimental conditions while we also pay attention to proper offset correction of the traces, which can be particularly tricky for the measurement of the input coherent state. That gives us a homodyne tomogram like the one shown in Fig. 9. From this we reconstruct an estimate of the underlying quantum state using the maximum likelihood method [4]. As mentioned in the Methods section, we correct for the non-perfect detector efficiencies in order to get the most accurate characterization of the protocol.

The phase values in the figure indicate the relative phase between the local oscillator and the OPO-injected probe beam. The probe beam is locked to the squeezed quadrature of the PSSV state, and Alice's input coherent beam is locked at  $90^\circ$  to the probe beam. Since we define our phase space in such a way that the anti-squeezing is aligned along the  $x$ -axis and the input states have real amplitudes (i.e. also along the  $x$ -axis), the  $90^\circ$  phase of the LO should correspond to the  $x$ -quadrature. We therefore rotate the reconstructed quantum state by  $-90^\circ$  in phase space - the free choice of global phase.

#### Appendix F: Modelling of qubit teleportation

To simulate the performance of our tele-amplifier setup in the case where the input is an arbitrary coherent state qubit

$$|\psi(\alpha, \theta, \phi)\rangle = \cos\frac{\theta}{2} |\Phi_+(\alpha)\rangle + e^{i\phi} \sin\frac{\theta}{2} |\Phi_-(\alpha)\rangle, \quad (\text{F1})$$

we set up a model for the protocol, using Wigner function formalism.

As the input state to be teleported, we took a pure qubit state of the above form. The initial resource state was a squeezed vacuum state with appropriate squeezing levels. In the experiment, the squeezed vacuum state within the homodyne-observed mode  $f_{\text{HD,out}}(t)$  is not pure. The impurity due to this mode selection can be modelled quite well by propagating the initially pure squeezed vacuum through a 92% transmission beam-splitter. The losses suffered by the photon-subtracted squeezed vacuum were similarly modelled by virtual beam-splitters, taking account of the 96% escape efficiency of the OPO, the 5% tapping ratio for the photon subtraction, and the 95% propagation efficiency towards the separating beam-splitter. Alice's detector was modelled as an on/off detector with 10% efficiency, roughly corresponding to our APD's detection efficiency and the transmission of the spectral filters.

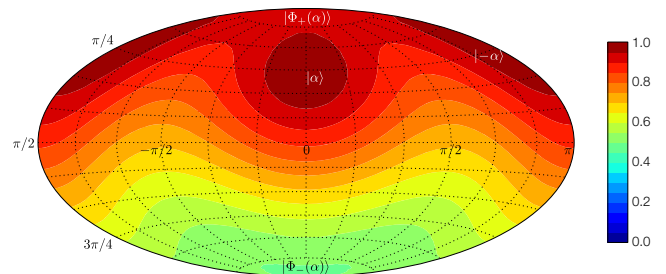


FIG. 10: Bloch sphere map of the fidelities between modelled and targeted outcomes of the  $|\psi(\alpha, \theta, \phi)\rangle \rightarrow |\psi(\alpha', \theta, \phi)\rangle$  tele-amplification, in this case for  $\alpha = 0.4$  and  $\alpha' = 0.6$ . The averaged fidelity here is 77%.

For a given input amplitude  $\alpha$  and desired output amplitude  $\alpha'$ , we simulate the tele-amplification process for 168 evenly distributed qubit states on the  $(\theta, \phi)$  Bloch sphere and calculate the fidelity between the output states and the targeted states  $|\psi(\alpha', \theta, \phi)\rangle$ . This results in a “fidelity map” like the one in Fig. 10 for every  $(\alpha, \alpha')$  setting. It is clear that the teleportation works best for coherent state inputs (near 100% fidelity) and for states near the North Pole (which is the even cat) and not very well for states near the South Pole (odd cat). By averaging over the Bloch sphere, we obtain an average fidelity for the outcomes of the protocol for the given  $(\alpha, \alpha')$  pair, giving one value for the average fidelity plot in Fig. 3.

---

- [1]Chefles, A. and Barnett, S. M. Optimum unambiguous discrimination between linearly independent symmetric states. *Phys. Lett. A* **250**, 223–229 (1998).
- [2]Mølmer, K. Non-Gaussian states from continuous-wave Gaussian light sources. *Phys. Rev. A* **73**, 063804 (2006).
- [3]Nielsen, A. E. B. and Mølmer, K. Single-photon-state generation from a continuous-wave nondegenerate optical parametric oscillator. *Phys. Rev. A* **75**, 023806 (2007).
- [4]Lvovsky, A. I. Iterative maximum-likelihood reconstruction in quantum homodyne tomography. *J. Opt. B: Quantum Semiclass. Opt.* **6**, S556–S559 (2004).